2009 IEEE/ASME International Conference on Advanced Intelligent Mechatronics
Suntec Convention and Exhibition Center
Singapore, July 14-17, 2009

Magnetic Field-Based Multi-DOF Orientation Sensor for PM-Based Spherical Actuators

Shaohui Foong, *Student Member, IEEE/ASME,* and Kok-Meng Lee, *Fellow, IEEE/ASME*

***Abstract*—Magnetic sensors have been utilized to locate the orientation and position of solitary permanent magnets (PM) through characterization of its unique nonlinear magnetic field. Similar characterization can be applied to the existing symmetric assembly of multiple PMs in the rotors of PM-based spherical actuators. This paper introduces a sensing method that exploits the symmetry of the rotor PM configuration to reduce the required characterization through discretization and classification of the global magnetic flux density mapping into smaller segments and sectors. Unlike existing methods that use fitted analytical models to extract orientation estimates, this method engages a trained neural network.**

I. Introduction

Multi-DOF electromagnetic spherical actuators rely on the magnetic force (and subsequent torques) provided through meticulous interaction between high-coercive rare-earth permanent magnets (PMs) mounted on the moving rotor and electromagnets (EMs) affixed on the stator for motion control. The demand for high precision multi-axis actuators capable of smooth manipulation for a multitude of medical, automation, manufacturing and robotics applications necessitates a sound position/orientation sensing system.

The premise of non-contact sensing solutions, which eliminate constraining friction and inertia, has motivated optical [1] and vision [2] based methods for measuring 3-DOF orientation of a spherical body. Such image-based sensors however are limited to low speed measurements and optical sensors require specially treated surfaces. Magnetic sensors have benefitted from miniaturization and a wealth of sensing techniques and possess small physical footprints and high sensitivity [3] which makes them an ideal choice for sensing operations in electromagnetic devices.

Magnetic sensors been used to trace and track orientation and position of an individual PM. In [4][5] and [6], 2-D sensor arrays were successfully used to track a PM by exploiting the unique magnetic field of the PM as measured simultaneously by all sensors at various orientation and position. Computation of the PM's position is achieved using a nonlinear optimization algorithm to minimize the deviation between measured and calculated magnetic field (using a single dipole analytical model). This approach is relatively slow, high in complexity and requires a good initial guess of the parameters. The concurrent use of sinusoidally magnetized ring shaped PMs with low cost hall-effect sensors have been utilized as an absolute single DOF rotary position sensor as discussed in [7] and [8]. Both approaches involve measuring the amplitude and direction of the magnetic field in the radial direction to infer the angular position of the PM.

More recently, Son and Lee used the distributed multipole (DMP) model to characterize the magnetic field of a single PM and design a magnetic field-based multi-DOF orientation sensor using methodically placed sensors [9]. One method discussed involved extraction of the PM orientation by expressing the measured magnetic field density as a polynomial function and solving the inverse problem. This paper acknowledges that existing PMs on spherical actuators can be harnessed for sensing purposes at no cost as described in [10], where the spin of a spherical rotor is perceived through variation in the magnetic field of the rotor PMs, and extends the characterization of the magnetic field to a symmetrical multiple-PM configuration for multi-DOF sensing. The presence of symmetry is a double-edged sword, dramatically reducing the required initial magnetic field characterization range while inadvertently introducing non-uniqueness during orientation inverse computation. As a result of this lack of uniqueness, the sensing system will be absolute locally and incremental globally.

The remaining of this paper offers the following:

- We present a method that capitalizes on the existing embedded symmetric assembly of permanent magnets (PMs) used for actuation of multi-DOF electromagnetic mechanisms for non-contact orientation sensing.
- This approach relies on using a network of field based sensors to detect variation in magnetic fields invoked by the moving PM configuration. As a result of the symmetric assembly, only a fraction of the entire desired range of motion is required for characterization. The DMP model provides analytical simulation of the nonlinear magnetic fields which are mapped to orientation estimates using an artificial neural network (ANN).
- This sensing method is validated with a sample trajectory and subsequent error analysis using a spherical motor as an illustrative example. The techniques conveyed here however are applicable to other PM-based actuators and sensing systems.

Manuscript received February 15, 2009. This work was supported in part by the Korea Institute of Machinery and Materials (KIMM), in part by the Georgia Agricultural Technology Research Program (ATRP), and in part by the U.S. Poultry & Egg Association.

S. Foong and K.-M. Lee are with the Woodruff School of Mechanical Engineering at the Georgia Institute of Technology, Atlanta, GA 30332-0405 USA (e-mail: shao@gatech.edu; kokmeng.lee@me.gatech.edu).

II. PM-Based Orientation Sensing System

Fig. 1 shows a model of a spherical actuator [11] where PMs and EMs are spaced equally on layers of circular planes such that their magnetization axes pass radially through the motor center. In addition, they are grouped in pairs; every two magnetic pole pairs form a plane providing symmetrical electromechanical forces. It is desired to design a position sensing system that acquires the orientation of the rotor through measurement of the moving magnetic field of the PMs on the rotor.

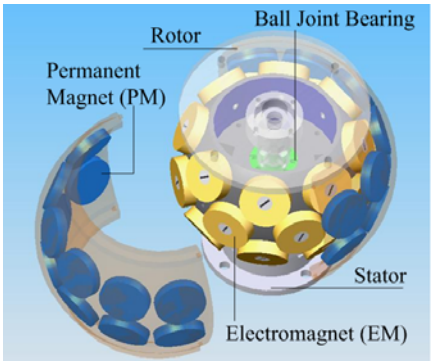

Fig. 1. CAD model of spherical actuator with PMs and EMs [11].

A. Stator & Sensors Placement

Fig. 2 defines the coordinate systems of the stator, rotor and orientation sensors, which are denoted as *XYZ* (reference), *xyz* (moving), and $X_pY_pZ_p$ (fixed local) respectively. The stator contains s sensors (blue circles) spaced equally along a circular path **C** of radius R_s in the fixed *XY* plane. The position of the p^{th} sensor in the *XYZ* plane is

$$\mathbf{S_p} = R_s\left[\cos\left((p-1)\psi_s\right) \quad \sin\left((p-1)\psi_s\right) \quad 0\right]^T \tag{1}$$

where p=1,2,…, s; and $\psi_s = 2\pi/s$ is the angular spacing between adjacent sensors. The coordinate transformation from the stator reference frame to the p^{th} sensor frame can be described by

$$\left[X_p \quad Y_p \quad Z_p\right]^T = \mathbf{\Gamma}_p\left((p-1)\psi_s\right)\left[X - R_s \quad Y \quad Z\right]^T \tag{2}$$

where $\mathbf{\Gamma}_p$ is the corresponding transformation matrix.

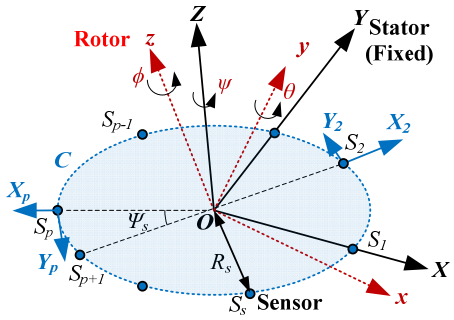

Fig. 2. Coordinate systems of rotor, stator and sensors.

B. Rotor & PMs Placement

The rotor is composed of multiple layers of cylindrical PMs (axially magnetized with radius a and length l), but without loss of generality, the following analysis is focused to 2 layers of PMs that are fixed onto the moving *xyz* frame. This *xyz* frame is rotated in space by a sequence of body fixed rotations about *Z*, *y* and finally *z* axis (*zyz* Euler rotation) by the corresponding angles of ψ, θ and ϕ respectively and this transformation can represented by

$$\left[x \quad y \quad z\right]^T = \mathbf{\Gamma}(\psi,\theta,\phi)\left[X \quad Y \quad Z\right]^T \tag{3}$$

The centroid location of the e^{th} PM on the ± layer (each containing f PMs) on the rotor expressed in Cartesian coordinates in the xyz frame using spherical angles as depicted in Fig. 3(a) is:

$$\mathbf{PM}_{e\pm} = R_{PM}\left[\cos\phi_e\cos\theta_\pm \quad \sin\phi_e\cos\theta_\pm \quad \sin\theta_\pm\right]^T \tag{4a}$$

$$\phi_e = \left(e - 1/2\right)\phi_{PM}\,,\ \phi_{PM} = 2\pi/f \tag{4b}$$

$$\theta_\pm = \pm\theta_L/2 \tag{4c}$$

where ϕ_{PM} is the azimuth spacing between adjacent PMs in each layer, θ_L is the zenith spacing between adjacent PM layers, R_{PM} is the radial distance of each PM from *O* and e=1,2,…,f. The requirement of an electromechanically balanced rotor and radial grouping of PMs stipulates that f must be an even integer. Each PM is orientated such that the magnetization axis, **M** passes through the origin *O*. In rotor coordinates this magnetization vector is given by:

$$\mathbf{r}_{e\pm} = \pm(-1)^e\left[\cos\phi_e\cos\theta_\pm \quad \sin\phi_e\cos\theta_\pm \quad \sin\theta_\pm\right]^T \tag{5}$$

Illustration of the zenith spacing and orientation of the PM and its magnetization vector in the *xz* plane is shown in Fig. 3b. Physical dimensions and positioning of the cylindrical PMs mandate restrictions on the azimuth and zenith spacing of the PMs and layers respectively due to possibility of physical interference. The minimum zenith and azimuth spacing are:

$$\theta_{L\min} = 2\tan^{-1}\left(a/\left(R_{PM} - l/2\right)\right) \tag{6a}$$

$$\phi_{PM\min} = 2\tan^{-1}\left(a/\left(R_{PM} - l/2\right)\cos\left(\theta_L/2\right)\right) \tag{6b}$$

The placement and orientation of PMs defined in (4) and (5) generates a distinct geometric pattern about the *z*-axis of the rotor. This pattern can be characterized by the azimuth spatial pitch of the rotor, Φ and is equal to $2\phi_{PM}$.

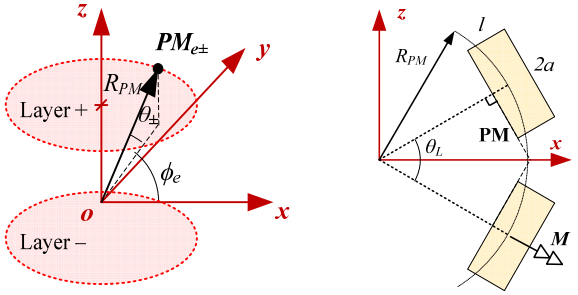

(a) Location of individual PMs. (b) Zenith spacing

Fig. 3. Rotor PM configuration.

C. Magnetic Flux Density Computation

The computation of the magnetic flux density of the PM as measured by a sensor is achieved using the distributed multipole (DMP) model [9][12]. The use of the DMP model is preferred because of its ability to characterize magnetic fields around PMs and EMs and are extendable to objects of other geometry. The magnetic flux density as measured by

the p^{th} sensor due to the e^{th} PM on the $\pm^{th}$ layer in the stator frame is given by $\mathbf{B}_{e\pm p}$. The details of this formulation can be found in the appendix. By superposition, the total magnetic flux density as measured in its respective coordinate system ($X_pY_pZ_p$) by the p^{th} sensor due to all PMs on both layers is

$$\mathbf{B}_p = \mathbf{\Gamma}_p^{-1}\left[\sum_{e=1}^{f}\mathbf{B}_{e+p} + \sum_{e=1}^{f}\mathbf{B}_{e-p}\right] \tag{7}$$

D. Absolute/Incremental Sensing Algorithm

The orientation sensing algorithm derived here harnesses and exploits the symmetric nature of the rotor/PM physical structure and sensor placement to reduce the required magnetic field characterization mapping to obtain the vector containing Eulerian angles $\boldsymbol{q}=[\psi,\theta,\phi]^T$. A range of inclination of the rotor is assumed and is limited to $-\theta_{\max} \le \theta \le \theta_{\max}$. Due to the spatial circular distribution of the sensors, the magnetic flux density is only unique for $-\psi_s/2 \le \theta \le \psi_s/2$, $-\theta_{\max} \le \theta \le \theta_{\max}$ and $-\Phi/2 \le \phi \le \Phi/2$. A mapping between this 3-D volume and $\boldsymbol{q}$ can be constructed and classified using the signs and magnitudes of orthogonal measurements from multiple sensors. Because of the complexity of visually illustrating a 3-D volume mapping and similarity of both approaches, a 2-D surface mapping is presented for clarity.

Assuming that ψ is an integer multiple of ψ_s, at least one sensor will be coincident with the x-axis of the rotor when $\theta=\phi=0$. The magnetic flux density measurements by this sensor (denoted as p'^{th} sensor) can be used for computation of the orientation angles of the rotor. This sensing algorithm can be summarized by the flowchart in Fig. 4. Due to the spatial pattern of Φ and alternating magnetization axis of adjacent PMs as characterized in (4) and (5), the 2-D global surface map the magnetic flux density for all 3 axis ($X_{p'},Y_{p'},Z_{p'}$) as a function of θ and ϕ as measured by the p'^{th} sensor can be divided into $2\pi/\Phi$ equal segments and further partitioned into smaller sectors within each segment. A trained neural network is used to locate the localized position within a sector surface map using the magnitude of the measurements while inspection of the sign of the measurements identifies the correct sector within the segment. Both sets of information are fused through sector transformation to obtain localized position within a surface map segment. Lastly a segment indexer determines the appropriate segment on the global surface map.

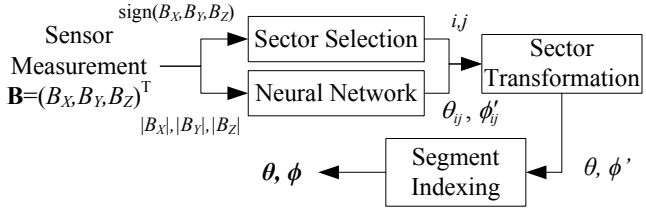

Fig. 4. Flowchart for inverse computation of θ and ϕ.

The DMP model and (7) allows the construction of a localized segment of the 2-D surface of the magnetic flux density for all 3 axis ($X_{p'},Y_{p'},Z_{p'}$) for $-\theta_{\max} \le \theta \le \theta_{\max}$ and $-\Phi/2 \le \phi' \le \Phi/2$. Employing the signs of $B_{X\,p'}$, $B_{Y\,p'}$, $B_{Z\,p'}$, as binary bits (positive=1, negative=0), this surface map segment can be further segregated into 2^3 sectors as described by Fig. 5. The red plus and blue minus symbols represent direction of the magnetic flux density for B_X, B_Y and B_Z of the p' sensor within each of the 8 sectors of the surface map segment. It is observed that the signs of B_X, B_Y and B_Z uniquely identifies the sector.

Hence an orientation estimate of the rotor requires at least three orthogonal field measurements. Although this might seem to require the implementation of 3-axis magnetic sensors, the symmetry in the rotor allows the operation of single axis magnetic sensors by recognizing that measurements by sensors on **C** are related by a known phase shift. For example, the measurement of the B_Z axis of any sensor is equal to the corresponding measurement of the sensor directly opposite it.

The magnitude of the surface map within each sector is related to the $\theta\phi'$ axes of to the surface map segment through the following coordinate sector transformation:

$$\begin{bmatrix}\theta\\ \phi'\end{bmatrix} = \begin{bmatrix}(-1)^i & 0\\ 0 & (-1)^j\end{bmatrix}\begin{bmatrix}\theta_{ij}\\ \phi'_{ij}\end{bmatrix} + \begin{bmatrix}0\\ \delta_j\end{bmatrix}\frac{\Phi}{2} \tag{8}$$

where $$\delta_j = \begin{cases}-1 & \text{if } j=0\\ 1 & \text{if } j=3\\ 0 & \text{otherwise}\end{cases}$$

and θ_{ij} and ϕ'_{ij} are the coordinate axes of the ij^{th} sector for $0 \le i \le 1$ and $0 \le j \le 3$. The conclusion from Fig. 5 and (8) is that the magnetic field mapping of only any *one* of the eight sectors is required to completely describe the entire segment and hence the global surface. The ratio of the area any single sector map to the area of the global surface is $\Phi/(16\pi)$. For simplicity, the sector whose coordinate axes coincides with the axes of the segment (highlighted in red in Fig. 5) is used.

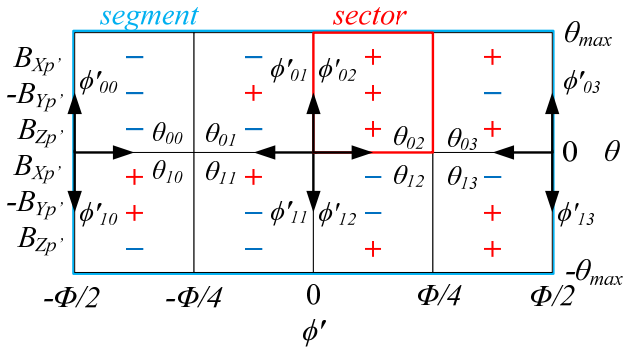

Fig. 5. Two-dimensional segment and sector mapping of $\mathbf{B}(\theta,\phi')$ at sensor p'.

A two-layer feed-forward artificial neural network (ANN) with h sigmoid hidden neurons utilizing the Levenberg-Marquardt supervised back propagation algorithm is trained to extract θ_{ij} and ϕ'_{ij} given the sector surface map for B_X, B_Y and B_Z. The input sector surface is discretized into a $N\times N$ grid resulting to total of N^2 training-target sets; 80% of the sets will be used for training, 15% for validation and 5% for

testing. For this application, the h hidden nodes neural network has 3 inputs and 2 outputs and can be mathematically represented in (9)

$$\left[\hat{\theta}_v \quad \hat{\phi}'_v\right]^T = \mathbf{NN}_h\left(\left[\left|B_{Xp}(v)\right|, \left|B_{Yp}(v)\right|, \left|B_{Zp}(v)\right|\right]\right) \tag{9}$$

where v is an integer representing the training set index ($1 \le v \le N^2$) and $\hat{\theta}$ and $\hat{\phi}'$ are the angular estimates of the neural network. The mean squared error (MSE) is used to evaluate of the performance of a neural network and is expressed as:

$$\text{MSE} = \frac{1}{N^2}\sum_{v=1}^{N^2}\left[\left(\theta_v - \hat{\theta}_v\right)^2 + \left(\phi'_v - \hat{\phi}'_v\right)^2\right] \tag{10}$$

The presence of multiple segments necessitates the inclusion of an indexer to keep track of the incremental count of Φ (or segments). The global expression for ϕ is

$$\phi(kT) = \phi'(kT) + w(kT)\Phi \tag{11}$$

where T is the sampling time of the sensor and w is an integer representing the current index. The index w is computed by ensuring the following inequality holds

$$\left|\phi(kT) - \phi((k-1)T)\right| \le \Phi/2 \tag{12a}$$

To prevent aliasing of the indexer, the spin rate $\dot{\phi}$ and sampling time of the sensor must satisfy the following:

$$\dot{\phi} < \Phi/2T \tag{12b}$$

The 2-D surface mapping can be extended to a corresponding volume mapping by noting that in 3-D, the segment (now a volume) can be divided into 2^4 sectors (volumes). Therefore while the 2-D surface mapping requires a minimum of 3 orthogonal sensor measurements, the corresponding 3-D volume mapping would require a minimum of 4 single axis sensor measurements. Hence even with 3-axis magnetic sensors, the simultaneous analysis of more than one sensor location is required for complete characterization.

III. Numerical Analysis

In order to facilitate illustration of the PM-based orientation measuring system, an existing spherical motor [11] consisting of 2 PM layers on the rotor each with 12 PMs is used as a platform for analysis. The magnetic sensors are installed in the center of each of the 8 EMs on the equatorial EM layer to create an actuator-sensor pair. In actual control implementation, the EMs (which are at known positions and orientations from each sensor) induce independent magnetic fields that can be compensated at each sensor using knowledge of the input current to the EMs [11]. Each cylindrical PM has a radius of 1.59 cm and is 0.635 cm long. They are modeled using a 4 loop and 10 dipoles DMP model as summarized in Table 1.

Table 1. PM and DMP model parameters.

PM:	**DMP:** (k=4,n=10);
M=1.31T, a = 1.59 cm, l = 0.635 cm	$\bar{\ell}$ = 0.191 cm m_o = 33.5 x 10^{-6} A/m, m_{1i} = 24.5 x 10^{-6} A/m m_{2i} = 57.6 x 10^{-6} A/m, m_{3i} = 52.0 x 10^{-6} A/m m_{4i} = 276 x 10^{-6} A/m

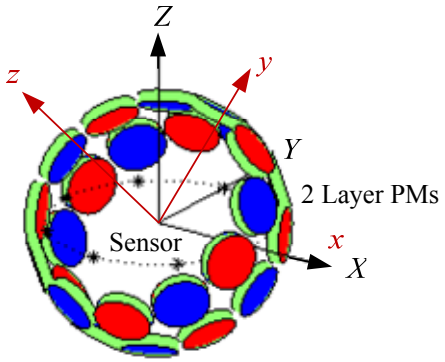

Fig. 6. Sensor and PM positioning in Cartesian coordinates.

A 3-D visual illustration of the positioning of the sensors and PMs on the rotor is shown in Fig. 6 using the parameters in Table 2. The blue and red surfaces of the cylindrical PM represent the north and south magnetic surfaces while the black asterisks represent the position of all 8 sensors. The desired range of motion of the rotor is $-\theta_{\max} \le \theta \le \theta_{\max}, -\infty \le \phi \le \infty$. A 2-D placement of the PMs and sensors in terms of the zenith and azimuth angles is shown in Fig. 7. Due to symmetric nature of the PMs, only half of the configuration is shown as the following half is identical. This figure allows easy interpretation of the entire configuration of the 24 PMs which is composed from 6 segments (Φ=60°) of a single 4 PM pattern encircled in green in Fig. 7.

Table 2. Sensor and PM parameters.

Sensor	s=8, R_s = 6.16 cm, γ_s = 45°, T=0.1 sec
PM	f = 12, R_{PM}=6.80 cm, ϕ_{PM}=θ_L=2θ_{max}=30°, Φ=60°

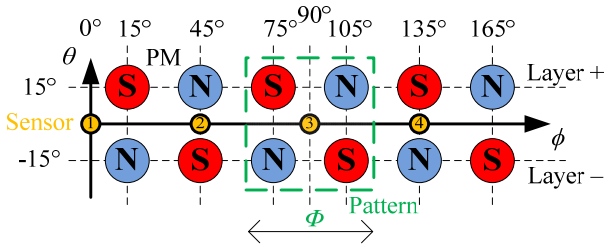

Fig. 7. Sensor and PM positioning in spherical coordinates

A. Magnetic Flux Density Surface Map Segment

Assuming ψ=0, the localized 2-D contour surface map segment of the magnetic flux density for all 3 axis as a function of θ and ϕ' as measured by S_1 is reproduced in Fig. 8. The lighter and darker regions represent areas of positive and negative values. It can be visually verified that the three surface maps adhere to the segregation in Fig. 5 and only 1/8 of the surface is unique and the remaining surface can be obtained by applying the transformation in (8). In fact, only 2% of the global surface map is required for characterization. Using the map described by Fig. 5, the 02th sector enclosed by the region $0 \le \theta \le \Phi/4 = 15°$ and $0 \le \phi' \le \Phi/4 = 15°$ is chosen to be characterized using the neural network. A surface plot of the magnetic flux density for all 3 axes for this sector is shown in Fig. 9.

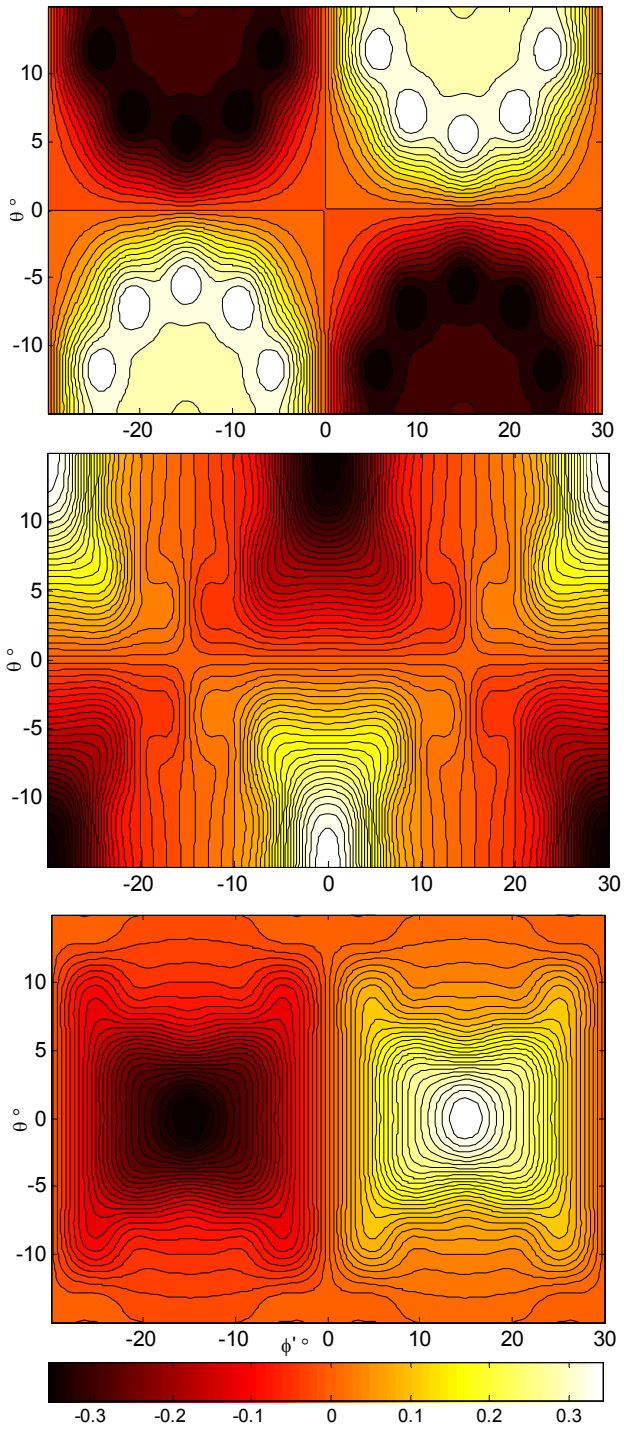

Fig. 8. Contour map of magnetic flux density segment at S_1. (B_{X1} top, B_{Y1} middle and B_{Z1} bottom. Units: Tesla)

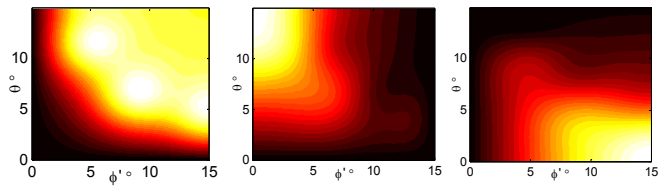

B_{X1} $-B_{Y1}$ B_{Z1}

Fig. 9. 2-D Surface map of magnetic flux density at 02th sector.

B. *Neural Network Characterization of Surface Sector*

Two-layer neural networks with varying number of hidden nodes are used to characterize the mapping between the sector surfaces of each of the 3 axis of the measured magnetic flux density to the angular estimates of θ and ϕ'. Each surface in Fig. 9 is discretized into a square 100×100 grid (0.15° spatial resolution) to produce 10000 pairs of training sets. The MSE of the ANN angular estimates of θ and ϕ' in logarithmic scale are shown as a function of the number of hidden nodes in Fig. 10. Increasing the number of nodes generally reduces the MSE and for 10000 training sets, the MSE converges to 10^{-2} deg^2 when h=70.

The angular error of the estimates of θ and ϕ' of the neural networks at each training set is compiled in Fig. 11(a) and (b) respectively for h=5, 20 and 70. As suggested by the plots, increasing the number of hidden nodes reduces the angular error across the entire sample set. A spatial distribution of the absolute angular error across the sector surface is shown in a 3-D plot in Fig. 11(c). For the network with 70 hidden nodes, the absolute errors for both angle estimates throughout the surfaces are less than 1.5° and over 90% of the surface has an absolute error less than 0.5°. The peaks in Fig. 11(c) reflect the high spatial nonlinearity of the magnetic field in a small localized area and can be arrested using multi-layer ANN at a penalty of computation time.

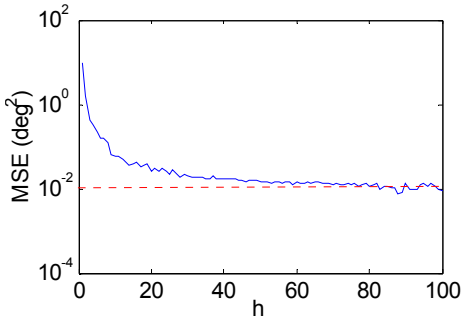

Fig. 10. MSE of angular estimates using different neural networks.

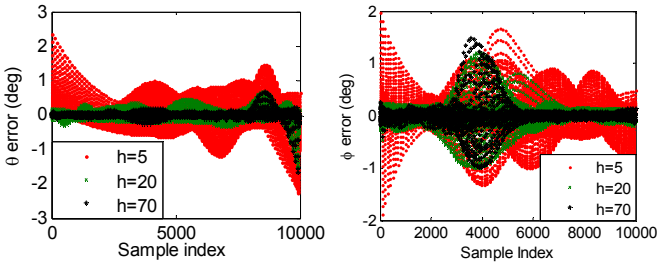

(a) Error of $\hat{\theta}$ at each sample. (b) Error of $\hat{\phi}'$ at each sample.

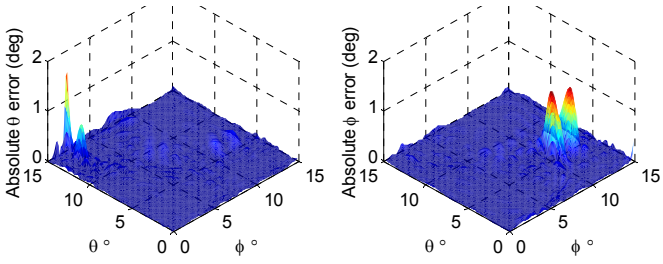

(c) Spatial distribution of $\left|\hat{\theta}-\theta\right|$ (left) and $\left|\hat{\phi}'-\phi'\right|$ (right). (h=70)

Fig. 11. Error analysis of different neural networks.

C. Trajectory Tracking

The sensing algorithm is tested by simulating the magnetic field of the rotor undergoing a known trajectory. A straight forward motion that ensures that 3 consecutive segments and all 8 sectors are tested is the following sinusoidal trajectory:

$$\begin{cases} \phi(t) = \pi t / 4 \\ \theta(t) = \left(\theta_{\max} \sin 2\phi\right) / 2 \end{cases} \tag{13}$$

Alternatively, this trajectory can be visually represented in the 2-D surface map as shown in the red arrow in Fig. 12.

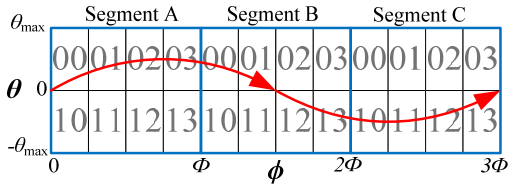

Fig. 12. 2-D representation of simulated trajectory.

The simulated trajectory and estimated position of the rotor obtained through the sensing algorithm (assisted by a neural network of 70 hidden nodes) and 3-axis sensor with sampling rate of 10 Hz are shown in Fig. 13(a). The corresponding errors of both angle estimates are plotted in Fig. 13(b). Except at 4 extreme points where the absolute error of the estimate of ϕ is 0.43°, the absolute errors for the remaining estimates of both angles are less than 0.1° throughout the entire trajectory.

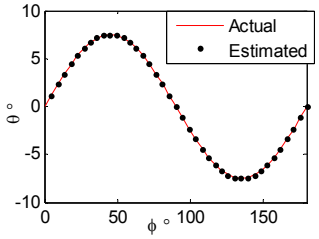

(a) Comparison between actual and estimated rotor position.

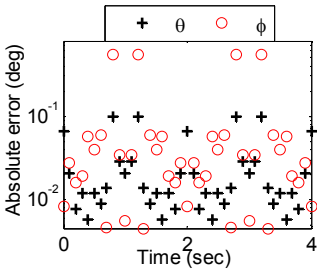

(b) Absolute error of estimated angles.

Fig. 13. Trajectory simulation and error analysis.

IV. Conclusion

We have presented a sensing method to measure the orientation of a pre-defined symmetric configuration of PMs. This method extends the characterization of the variation in magnetic field to include multiple PMs and exploits the symmetry of the rotors to divide the range of motion into segments and sectors, thereby reducing the characterization requirement to just a single sector. A trained ANN is used to identify the location within a sector and inspection of the direction of measured magnetic flux density is used to identify the appropriate sector. An indexer is used to incrementally count the motion of the segments. Using a spherical motor as a platform for illustration and basis for numerical analysis, the sensing error associated with using an ANN to characterize the nonlinear magnetic fields was investigated.

Appendix

The cylindrical PM is modeled analytically with the DMP model [9][12] using k circular loops (each with radius $\bar{a}_j$, j = 0,…, k) of n dipoles (strength m_j) in parallel to its magnetization vector. A dipole is defined as a pair of source and sink separated by a distance $\bar{\ell}$ ($0 < \bar{\ell} < \ell$). The coordinates of the source and sink of the e^{th} PM on the $\pm^{th}$ layer, $\mathbf{P}_{\pm eji+}$ and $\mathbf{P}_{\pm eji-}$ respectively, are known in XYZ frame. R_{ji+} and R_{ji-} are the distances from the i^{th} dipole in j^{th} loop, to a sensor $\boldsymbol{S}_p$. In XYZ frame, the magnetic flux density $\mathbf{B}_{e\pm}$ as measured by the p^{th} sensor due to the e^{th} PM on the $\pm^{th}$ layer is:

$$\mathbf{B}_{e\pm p} = \frac{\mu_o}{4\pi} \sum_{j=0}^{k} m_j \sum_{i=1}^{n} \left(\frac{\mathbf{A}_{R\pm eji+}}{R_{\pm eji+}^2} - \frac{\mathbf{A}_{R\pm eji-}}{R_{\pm eji-}^2} \right) \tag{A1}$$

where $R_{\pm eji\pm} = \left| \mathbf{S_P} - \mathbf{P}_{\pm eji\pm} \right|$; $\dfrac{\mathbf{A}_{R\pm eji\pm}}{R_{\pm eji\pm}^2} = -\dfrac{\mathbf{S_P} - \mathbf{P}_{\pm eji\pm}}{\left| \mathbf{S_P} - \mathbf{P}_{\pm eji\pm} \right|^3}$

Acknowledgment

This work was supported in part by the Korea Institute of Machinery and Materials (KIMM), in part by the Georgia Agricultural Technology Research Program (ATRP), and in part by the U.S. Poultry & Egg Association.

References

[1] K.-M. Lee and D. Zhou, "A Real-Time Optical Sensor for Simultaneous Measurement of Three-DOF Motions," *IEEE/ASME Transactions on Mechatronics*, vol. 9, no. 3, pp. 499-507, Sep 2004.

[2] H. Garner, M. Klement, and K.-M. Lee, "Design and Analysis of an Absolute Non-Contact Orientation Sensor for Wrist Motion Control," *Proceedings of IEEE/ASME International Conference on Advanced Intelligent Mechatronics*, Jul 2001.

[3] J. Lenz and A. S. Edelstein, "Magnetic Sensors and Their Applications," *IEEE Sensors Journal*, vol. 6, no.3, pp. 631-649, 2006.

[4] C. Hu, M. Q.-H. Meng, M. Mandal and X. Wang, "3-Axis Magnetic Sensor Array system for Tracking Magnet's Position and Orientation," *Proceedings of 6th World Congress on Intelligent Control and Automation*, Jun 2006.

[5] V. Schlageter, P.-A. Besse, R. S. Popovic, and P. Kucera, "Tracking System with Five Degrees of Freedom Using a 2D-Array of Hall Sensors and a Permanent Magnet," *Sensors and Actuators, A: Physical*, vol. 92, no. 1-3, pp. 37-42, Aug 2001.

[6] J. T. Sherman, J. K. Lubkert, R. S. Popovic, and M. R. DiSilvestro, "Characterization of a Novel Magnetic Tracking System," *IEEE Transactions on Magnetics*, vol. 43, no. 6, pp. 2725-2727, Jun 2007.

[7] J. J. H. Paulides, E. A. Lomonova, A. J. A. Vandenput and E.H. Zaaijer, "Sinusoidal Behavior of a Dipole Magnetization for Position Sensing Applications," *IEERE Transactions on Magnetics*, vol. 42, no. 10, pp 3294-3296, Oct 2006

[8] S.-H. Jeong, S.-H. Rhyu, B.-I Kwon and B.-T Kim, "Design of the Rotary Magnetic Position Sensor with the Sinusodially Magnetized Permanent Magnet," *IEEE Transactions on Magnetics*, vol. 43, no. 4 pp. 1837-1840, Apr 2007.

[9] H. Son and K.-M. Lee, "Distributed Multipole Models for Design and Control of PM Actuators and Sensors," *IEEE/ASME Transactions on Mechatronics*, vol. 13, no 2, pp. 228-238, Apr 2008.

[10] C. K. Lim, and I. M. Chen, "A Novel 3-DOF Sensing Methodology for Spherical Actuator," *IEEE/ASME Advanced Intelligent Mechatronics*, pp. 1-6, Sep 2007.

[11] K.-M. Lee, K. Bai, J. Lim, "Dipole Models for Forward/Inverse Torque Computation of Spherical Motor," *IEEE/ASME Transactions on Mechatronics*, vol 14, no. 1, pp 46-54, Feb 2009.

[12] K.-M. Lee and H. Son, "Distributed Multipole Model for Design of Permanent-Magnet-based Actuators," *IEEE Transactions on Magnetics*, vol. 43, no. 10, pp. 3904–3913, Oct. 2007.